

# A first-order statistical exploration of the mathematical limits of Micromagnetic Tomography

Frenk Out<sup>1</sup>, David Cortés-Ortuno<sup>1</sup>, Karl Fabian<sup>2</sup>, Tristan van Leeuwen<sup>3,4</sup>,  
Lennart V. de Groot<sup>1</sup>

<sup>1</sup>Paleomagnetic laboratory Fort Hoofddijk, Department of Earth Sciences, Utrecht University,  
Budapestlaan 17, 3584 CD Utrecht, The Netherlands.

<sup>2</sup>Norwegian University of Science and Technology (NTNU), S. P. Andersens veg 15a, 7031 Trondheim,  
Norway

<sup>3</sup>Mathematical Institute, Faculty of Sciences, Utrecht University, Utrecht, The Netherlands

<sup>4</sup>Department of Computational Imaging, Centrum Wiskunde & Informatica (CWI), The Netherlands

## Key Points:

- The performance of Micromagnetic Tomography is tested against the sample's geometry, instrumental noise level and sampling interval
- The current experimental routine enables determining mathematically reliable magnetic moments for individual grains in natural samples
- Sample thickness and grain density are the prime factors controlling the uncertainty of magnetic moments of individual grains

## Abstract

The recently developed Micromagnetic Tomography (MMT) technique combines advances in high resolution scanning magnetometry and micro X-ray computed tomography. This allows precise recovery of magnetizations of individual magnetic grains in a sample using a least-squares inversion approach. Here we show that at least five factors are governing the mathematical validity of MMT solutions: grain concentration, thickness of the sample, size of the sample's surface, noise level in the magnetic scan, and sampling interval of the magnetic scan. To compute the influence of these parameters, we set up series of numerical models in which we assign dipole magnetizations to randomly placed grains. Then we assess how well their magnetizations are resolved as function of these parameters. We expanded the MMT inversion to also produce the covariance and standard deviations of the solutions, and use these to define a statistical uncertainty ratio and signal strength ratio for each solution. We show that the magnetizations of a majority of grains under realistic conditions are solved with very small uncertainties. However, increasing the grain density and sample thickness carry major challenges for the MMT inversions, demonstrated by uncertainties larger than 100% for some grains. Fortunately, we can use the signal strength ratio to extract grains with the most accurate solutions, even from these challenging models. Hereby we have developed a quick and objective routine to individually select the most reliable grains from MMT results. This will ultimately enable determining paleodirections and paleointensities from large subsets of grains in a sample using MMT.

## Plain Language Summary

Iron-bearing rocks have the ability to capture and store the direction and strength of Earth's magnetic field. This information is used to unravel the behavior of the magnetic field that protects us from harmful solar radiation. However, obtaining a reliable signal from these rocks is difficult using existing methods because many iron-oxide grains exhibit complex magnetic behavior and obscure the magnetic information in them. To determine magnetizations from individual grains, a new method known as Micromagnetic Tomography has been developed. This method works similarly to imaging techniques in hospitals, but now a thin slice of rock containing magnetic grains is scanned. By using computer models we discovered that Micromagnetic Tomography is able to reliably extract magnetic signals from a majority of grains in many rock samples. Addi-

50 tionally, we have developed two new parameters that help us to easily select the mag-  
51 netizations of the most reliable grains in a sample. In this way the signal of those grains  
52 can be effectively used to provide accurate information on the present and past state of  
53 the Earth's magnetic field.

## 1 Introduction

Obtaining a reliable characteristic remanent magnetization (ChRM) from volcanic rock samples is an important challenge in paleomagnetism. Volcanic rocks acquire a thermoremanent magnetization (TRM) when they cool in the Earth's magnetic field that is proportional to the direction and strength of the magnetic field at the time of cooling. TRMs of natural rocks are often regarded to be the most reliable data source for geomagnetic field models because of their ability to store information on the paleomagnetic field for thousands to millions of years (e.g. Panovska et al., 2019; Pavón-Carrasco et al., 2021). Full vector ChRMs consist of both directional and intensity information on the past geomagnetic field, but they can generally only be obtained for 10% to 20% of volcanic samples carrying TRMs (e.g. Tauxe & Yamazaki, 2015; Nagy et al., 2017). One of the reasons for the low success rates is that only single domain (SD) or pseudo-single domain (PSD) iron oxide grains, typically with diameters  $< 1 \mu\text{m}$ , are reliable recorders of the Earth's magnetic field. Larger multidomain (MD) grains are typically prone to more unstable magnetizations (Néel, 1955; Fabian, 2000, 2001). Natural rocks commonly contain a wide range of iron-oxide particle sizes. Magnetically adverse behaved MD grains are therefore often present. When measuring bulk rock samples the measured magnetic moment is a statistical summation of all the magnetic grains in the sample. The presence of MD grains therefore often explains the low success rate of extracting a reliable full vector bulk ChRM.

A solution to this problem would be to differentiate between signals stored in small and large grains by determining the magnetization of each iron-oxide grain in a sample separately. To obtain all individual magnetic moments, the magnetic flux above a thin sample produced by all grains inside is measured on a micrometer scale. Such a map of the magnetic flux with the necessary resolution in space and magnetization can be obtained from a scanning superconducting quantum interference device (SQUID; e.g. Egli & Heller, 2000; Weiss et al., 2007; de Groot et al., 2018) or a quantum diamond magnetometer (QDM; e.g. Glenn et al., 2017; Farchi et al., 2017; de Groot et al., 2021). Unfortunately, this is not sufficient to reconstruct the magnetic moments of individual grains inside the sample. To reduce the number of unknown variables in the inversion, the position of the magnetic grains must be constrained further. Weiss et al. (2007), for example, applied a constraint related to the dipolar magnetization of all grains, by assuming that the magnetization for all grains is uniform in intensity and direction. The magnetic

signal of grains close to the sensors that detect the surface magnetic field, however, is better modeled using multipoles than dipoles (Cortés-Ortuño et al., 2021). Additionally, since shapes and volumes of grains can vary, it appears unlikely that the magnetization of all grains are uniform in intensity and direction (Dunlop & Özdemir, 1997). To avoid further assumptions on the positions of grains, de Groot et al. (2018) employed micro X-Ray Computed Tomography (microCT) to exactly determine these positions. By combining microCT with the surface magnetic field obtained by magnetometry the resulting mathematical inversion problem becomes well posed (Fabian & De Groot, 2019), and it is possible to compute the individual magnetic moments of every grain in the sample. It was recently shown that not only the dipole component of the grain’s magnetic moments can be recovered, but also higher order multipole components can be determined (Cortés-Ortuño et al., 2021). This technique of combining scanning magnetometry data with microCT analyses to constrain the mathematical inversion and obtain magnetic moments of individual grains in a sample is now known as Micromagnetic Tomography (MMT).

de Groot et al. (2018) and de Groot et al. (2021) obtained solutions for the magnetizations of each grain in a synthetically fabricated magnetite sample containing 128 grains with an imposed laboratory magnetization, but did not analyze the validity of their solutions under the experimental conditions. Here, we assess the validity of MMT solutions by determining the relative size of the standard deviation of the magnetic moment, which can be produced by the inversion scheme. This is an important addition to the magnetic moment itself, because a relatively large standard deviation implies that the obtained magnetic moment is not very well resolved; while a relatively low standard deviation indicates a higher precision associated with the estimate of the magnetic moment.

We considered five different factors involved in the calculation of the individual magnetic moments that may substantially affect the uncertainty of MMT solutions: (1) the thickness of the sample, (2) the area covered by the surface magnetic scan, (3) the grain density of the rock sample, (4) the distance between adjacent measurement points on the surface, and (5) the instrumental noise level of the surface magnetometry. The aim of our study is to investigate the quality of individual grain magnetic moments obtained with MMT as a function of these five factors. There are undoubtedly more factors influencing the solution, such as grains not recognized by MicroCT, or co-registration errors related to spatial distortions between microCT data and magnetic field data. These

factors are challenging to model and depend primarily on the technical details and configurations of the instruments involved and are better and easier solved by a technical assessment than by mathematical corrections. For this reason we limit ourselves to the above five direct factors which either need to be taken into account in all inversion approaches, or directly help to optimize the general measurement setup. We design numerical models to cover all combinations of these five factors. Another limitation of our study is that we assign *dipolar* magnetic moments to all grains in our models; although multipole moments may be more realistic for the larger grains included (Cortés-Ortuño et al., 2021). Because higher multipole moments are only detectable at shallow depths (Cortés-Ortuño et al., 2021; de Groot et al., 2021), they appear to be too specific for this first study into the mathematical uncertainties and limitations of the new MMT technique. To determine the quality of the magnetic moments as determined by MMT in a spherical coordinate frame we define a 95% confidence interval that we obtain from bootstrapping the standard deviations in the  $x$ ,  $y$ , and  $z$ -directions. We choose this because standard deviations in the three orthogonal directions are difficult to directly convert to a spherical coordinate frame; while our 95% confidence interval gives a quantitative indication of the mathematical accuracy of the solution in a single parameter. Additionally, we evolve the  $V/R^3$ -ratio (Cortés-Ortuño et al., 2021) that relates the depth and volume of a grain to the strength of the magnetic signal that the grain can potentially produce on the surface of the sample, into the ‘signal strength ratio’. We then use this signal strength ratio (SSR) to quickly discern which grains are solved with high confidence. Finally, we discuss the implications of our results on obtaining highly accurate ChRM measurements.

## 2 Methods

### 2.1 Model design

The inversion routine we use here closely follows the procedure as described in de Groot et al. (2018, 2021), but we first define synthetic models given the five parameters that we consider in this study. This requires populating ‘sample volumes’ with grains in random locations and assign them a somewhat realistic magnetic moment. Then we calculate the map of the magnetic flux on the surface of the sample and perturb these maps with realistic noise. Once the sample volumes and magnetic flux map are determined we apply the inversion routine but also produce the standard deviations associ-

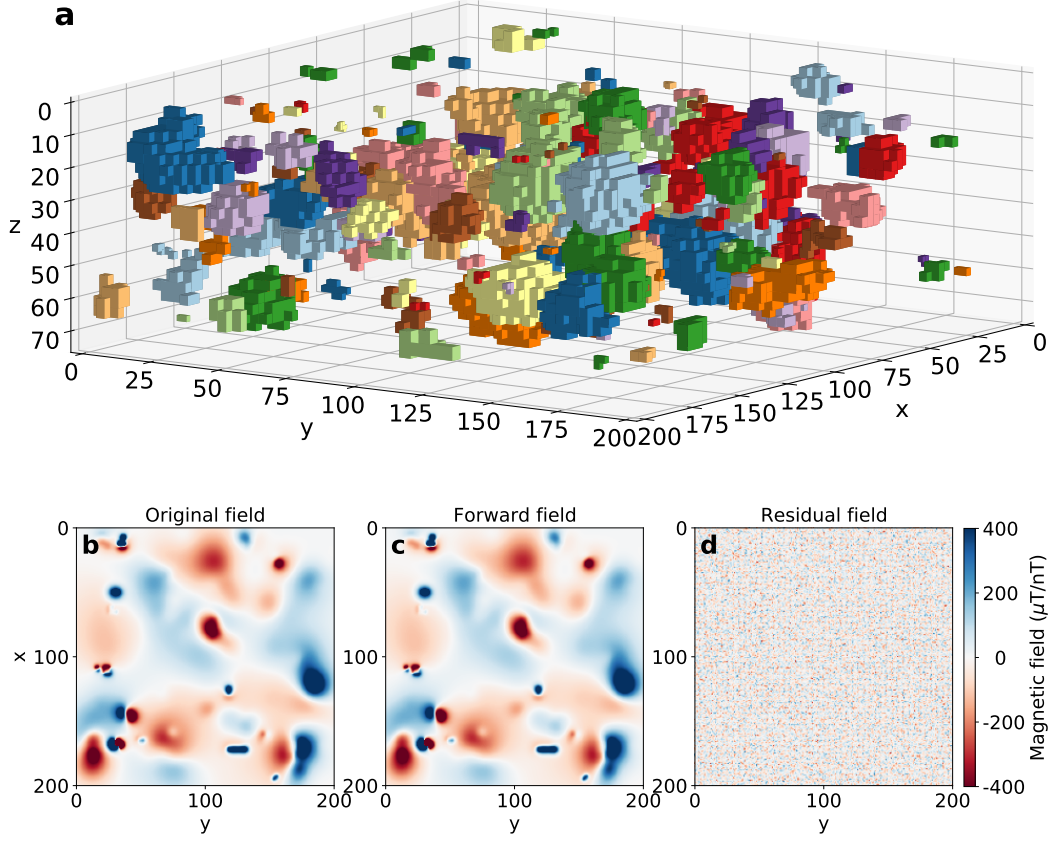


**Figure 1.** The MMT workflow of one of our models containing 75,000 grains per  $\text{mm}^3$  with a dipolar magnetization. a) Geometric overview of the model with a  $200 \times 200 \mu\text{m}^2$  sample surface size. Each grain is assigned a color for clarity, the colors do not have further meaning. The sensor grid is located on top of the model at  $z = 0$ . b) Original magnetic field created by the signal of the grains and after adding noise with a level of 100 nT. c) Magnetic field produced by the signal of grains with the inverted magnetization values. The unit of field strength in b) and c) is  $\mu\text{T}$ . d) Residual field obtained by subtracting the original field in b) from the forward field based on the inversion result in c). The unit of field strength in d) is nT.

**Table 1.** Parameters changed between models. Every possible combination of parameters is assessed in this study, resulting in 448 models. Each model is then ran 15 times to ensure statistically robust results.

Parameter	Unit	Modeled values
Sample surface size	$\mu\text{m}^2$	200×200, 500×500
Sample thickness	$\mu\text{m}$	50, 75
Grain density	$10^3$ grains per $\text{mm}^3$	2.5, 5.0, 10.0, 25.0 50.0, 75.0, 100.0
Sampling interval	$\mu\text{m}$	1, 2, 4, 5
Noise level	nT	5, 20, 50, 100

ated with the individual magnetic moments. Lastly, we define the 95% confidence interval of magnetic moments to assess the performance of MMT as a function of the five input parameters for the models.

### 2.1.1 Populating sample volumes

To define the input of the inversions we start with a rectangular sample volume with a predefined, rectangular, surface size and a set sample thickness. Inside this volume a number of modeled iron-oxide grains are randomly placed such that they do not intersect. The number and average volume of these grains determine the modeled iron-oxide grain density. We modeled samples with an area of  $200 \times 200$  and  $500 \times 500 \mu\text{m}^2$ . The maximum thickness of the models was either 50 or 75  $\mu\text{m}$  (Table 1). The individual grains used to populate the models with were taken from the actual geometries obtained from a microCT scan of a volcanic sample prepared from a sister sample of HW03 (de Groot et al., 2013; ter Maat et al., 2018; de Groot et al., 2021). This sample was obtained from a lava flow active in 1907 on Hawaii. The sample was drilled at an elevation of 603 m ( $\pm 4$  m) with a latitude of  $19^\circ 4.315'$  and a longitude of  $155^\circ 44.314'$ . The sample was reduced to a thickness of 80  $\mu\text{m}$ , after which the location and size of its magnetic grains were obtained with MicroCT. We populated the models with these grains until the respective grain density was reached, which is specified in Table 1. By using this range of grain densities, the models simulated both the low grain density of the synthetic sam-



ple of de Groot et al. (2018) and the high grain density of the volcanic sample of de Groot et al. (2021). Each grain was then placed at a random location within the model such that it does not intersect another grain or the boundaries of the model (Fig. 1a). To speed up the placing procedure of the grains in the model, we imposed that the top side of each grain could only be placed between the surface of the sample and 10  $\mu\text{m}$  from the bottom of the sample. If the grain did not fit at the given location, we retried placing the grain up to a hundred times. If the grain did not fit by then, we selected at random another grain geometry and tried to fit the new grain up to a hundred times again.

### 2.1.2 *Assigning realistic magnetizations*

In the next step, each grain was assigned a random magnetization  $\mathbf{m} = (m_x, m_y, m_z)$ , where  $|\mathbf{m}|$  denotes its magnitude. To obtain realistic magnetization values, the value of  $|\mathbf{m}|$  was chosen to agree with the magnetization versus grain diameter trend for a natural volcanic sample presented in Fig. 4D of de Groot et al. (2021). This trend is in good agreement to the relation between the relative magnetization as function of grain diameter in Fig. 29 of Dunlop (1990). The trend line in Fig. 4D (de Groot et al., 2021) can be converted to the empirical relation:

$$|\mathbf{m}| = m_0 (V/V_0)^\alpha, \quad (1)$$

where  $V_0$  is the volume, and  $m_0$  the magnetic moment of a sphere with diameter 1  $\mu\text{m}$ ;  $\alpha$  is the relation parameter, and  $|\mathbf{m}|$  is the absolute expected magnetic moment of a grain with volume  $V$ . For the trend line in Fig. 4D in de Groot et al. (2021) we obtained:  $m_0 = 46.5 \text{ kA/m}$ , and  $\alpha = -0.355$ . To simulate the spread in the data points that define this relation, we add a perturbation to the magnetizations. To this end the magnetization norm  $|\mathbf{m}|$  was multiplied by  $10^{N(\mu, \sigma^2)}$ , where  $N(\mu, \sigma)$  represents the Gaussian distribution with a mean,  $\mu$ , of zero and a variation,  $\sigma^2$ , of  $0.5^2$ , to produce the final magnetization norm  $|\mathbf{m}_f|$ . Hereafter, we sampled the uniform distribution  $U(0, 2\pi)$  to obtain the angle  $\phi$  of the magnetization vector in the  $x$ - $y$ -plane. The angle  $\theta$  with respect to the  $z$ -axis was sampled from the uniform distribution  $U(0, \pi)$ . The norm and the two angles of the magnetization vector were then transformed into the Cartesian components  $m_x$ ,  $m_y$ , and  $m_z$ .

### 2.1.3 Calculating the magnetic flux map

Once the particle positions and magnetizations are assigned, the grid of measurement points is defined on the surface  $z = 0$  by summing the resulting magnetic field on the surface arising from all grains in the sample. The sampling interval of the magnetic flux map is one of the parameters that we investigate in this study, so it is varied to represent different realistic sampling intervals (Table 1). The smallest sampling interval used in the analysis is  $1 \mu\text{m}$  such that a measurement area of  $200 \times 200 \mu\text{m}^2$  contains  $201 \times 201$  ( $=40,401$ ) measurement points, and a model area of  $500 \times 500 \mu\text{m}^2$  contains  $501 \times 501$  ( $=251,001$ ) measurement points. The largest sampling interval is set to  $5 \mu\text{m}$ , so that the  $200 \times 200 \mu\text{m}^2$  surface contains  $41 \times 41$  ( $=1,681$ ) data points and the  $500 \times 500 \mu\text{m}^2$  surface is limited to  $101 \times 101$  ( $=10,201$ ) data points.

With the position of the grains and measurement points we calculate the Green's matrix  $Q$ . The Green's matrix relates the magnetic signal that each grain contributes to the response of the signal at the surface of the sample. The size of the Green's matrix is dependent on the amount of grains and measurement points. If a model contains  $K$  grains and  $P$  measurement points, then the Green's matrix consists of  $3 \times K$  rows and  $P$  columns (see Supplementary Information of de Groot et al., 2018). By combining the magnetization of each grain  $\mathbf{m}_a$  with the Green's matrix, the magnetic signal  $\phi$  was obtained in a forward approach:

$$\phi = Q\mathbf{m}_a. \quad (2)$$

The magnetic signal at each measurement point is the total integrated magnetic flux from all modeled grains through a modeled rectangular sensor loop in the  $x$ - $y$ -plane of the sample with side lengths  $1 \times 1 \mu\text{m}$  centered at the measurement point. To simulate the effect of instrumental errors introduced by a magnetometer,  $\mathbf{e}$ , one of the four noise levels specified in Table 1 was added to the magnetic field of each model,  $\tilde{\phi} = \phi + \mathbf{e}$ . This adds white noise that is normally distributed with a standard deviation governed by the noise level and with a zero mean to the magnetic surface scan. These noise magnitudes are comparable to those described by Glenn et al. (2017). Now the maps of the magnetic flux at the surface of our models are known (Fig. 1b).

#### 2.1.4 Inversion procedure

Akin to de Groot et al. (2018), Fabian and De Groot (2019), and de Groot et al. (2021), we used a least-squares minimization to obtain the magnetization of individual grains in the sample, since the inverse problem has a larger number of magnetic flux field observations than unknown magnetization components, *i.e.*  $P > 3 \times K$  (Snieder & Trampert, 1999). The magnetization solution,  $\hat{\mathbf{m}}_a$ , is given by

$$\hat{\mathbf{m}}_a = Q^\dagger \tilde{\phi}, \quad (3)$$

with  $Q^\dagger$  being the pseudo-inverse of  $Q$ . The calculated magnetization is used to compute the forward magnetic flux field,  $\hat{\phi}$  (Fig. 1c). This forward field is obtained through matrix multiplication of the calculated magnetizations with the Green's matrix

$$\hat{\phi} = Q \hat{\mathbf{m}}_a. \quad (4)$$

Subtracting the initial magnetic field from the forward field results in the residual magnetic field (Fig. 1d).

#### 2.1.5 Varying the input parameters

For each of the five input parameters we determined a range of realistic values to assess (Table 1). Incorporating all combinations of these five factors yields 448 different computational models, formed by all possible combinations of 2 sample surface areas, 2 sample thicknesses, 7 different grain densities, 4 different sampling intervals, and 4 different noise levels. We executed each of these models fifteen times with different random grain locations and dipolar magnetizations to attain enough inversion solutions for a stable and meaningful statistical underpinning of the results. The coarser sampling rates of 2, 4, and 5  $\mu\text{m}$  grid spacing were simulated by sub-sampling the 1  $\mu\text{m}$  grid after noise was added. In this way we make sure that each sampling rate uses the same noise contaminated magnetic field.

## 2.2 Covariance and standard deviation

The inversion as used for MMT allows for determining the standard deviation and covariance associated with each solution. To assess the accuracy of the MMT results we define a 95% confidence interval based on bootstrapping the three orthogonal standard deviations for each solution that we obtain from the inversion routine. This is done such

that if we would repeat the inversion procedure and redraw the Gaussian noise  $\mathbf{e}$  a hundred times, we would expect for each grain that 95 out of the 100 associated 95% confidence intervals contain the ‘true’ correct magnetization,  $\mathbf{m}$  (Sim & Reid, 1999). The radius of the confidence interval gives the precision of the corresponding magnetization solution, where a larger radius indicates a less precise solution.

The 95% confidence interval is constructed by means of the magnetization solutions  $\hat{\mathbf{m}}_a$  and the standard deviations,  $\sigma_x$ ,  $\sigma_y$ , and  $\sigma_z$ . To obtain the standard deviations, the covariance matrix has to be constructed first. The covariance matrix  $C_{ij}$  is defined to indicate the expected relationship between two variables  $a$  and  $b$  relatively to the deviation from their expected values  $E[a]$  and  $E[b]$ . If the covariance between two magnetization variables  $m_1$  and  $m_2$  is positive, and if  $m_2$  is larger than expected, then this implies that  $m_1$  will be larger than expected and vice versa. Conversely, if the covariance is negative and if  $m_1$  is larger than expected, then this means that  $m_2$  will be smaller than the expected value and vice versa. The covariance of a magnetization variable with itself,  $C_{ii}$ , is always positive and indicates the squared deviation from the expected value, which is frequently called the squared standard deviation. To derive the standard deviation per magnetization component, we first define the covariance matrix as

$$C = E[(\hat{\mathbf{m}}_a - E[\mathbf{m}_a])(\hat{\mathbf{m}}_a - E[\mathbf{m}_a])^T]. \quad (5)$$

The value  $E[\mathbf{m}_a]$  is known as the expected magnetization, which is the magnetization that would result from perfect magnetic flux observations without any observational noise

$$E[\mathbf{m}_a] = Q^\dagger \phi \quad (6)$$

With the combination of equations 3 and 6, we can define  $\hat{\mathbf{m}}_a$  as the sum of perfect observations and instrumental errors, which is given by

$$\begin{aligned} \hat{\mathbf{m}}_a &= Q^\dagger(\phi + \mathbf{e}) \\ &= Q^\dagger \phi + Q^\dagger \mathbf{e} \\ &= E[\mathbf{m}_a] + Q^\dagger \mathbf{e}, \end{aligned} \quad (7)$$

with  $Q^\dagger \mathbf{e}$  being the magnetization error. Equation (5) is simplified to

$$\begin{aligned} C &= E[(E[\mathbf{m}_a] + Q^\dagger \mathbf{e} - E[\mathbf{m}_a])(E[\mathbf{m}_a] + Q^\dagger \mathbf{e} - E[\mathbf{m}_a])^T] \\ &= E[(Q^\dagger \mathbf{e})(Q^\dagger \mathbf{e})^T] \\ &= E[Q^\dagger \mathbf{e} \mathbf{e}^T (Q^\dagger)^T]. \end{aligned} \quad (8)$$

The matrix  $Q^\dagger$  is the least squares inverse of  $Q$ , therefore it is defined as  $(Q^T Q)^{-1} Q^T$  (Snieder & Trampert, 1999). The matrix is not a variable, therefore only the expected value of the errors of the magnetic field is left,  $E[\mathbf{e}\mathbf{e}^T]$ . If we assume that the errors are uncorrelated, then this expression is equal to the squared standard deviation times the unit matrix,  $\sigma^2 I$ . Note that this standard deviation is related to the expected instrumental noise in the data. Implementing this new expression into equation (8) and rearranging gives the final equation for calculating the covariance matrix

$$\begin{aligned} C &= Q^\dagger E[\mathbf{e}\mathbf{e}^T] (Q^\dagger)^T \\ &= Q^\dagger E[\mathbf{e}\mathbf{e}^T] ((Q^T Q)^{-1} Q^T)^T \\ &= (\sigma^2 (Q^T Q)^{-1})^T = \sigma^2 (Q^T Q)^{-1}. \end{aligned} \quad (9)$$

We deduced from equation (5) that the covariance matrix is symmetric. Hence,  $(\sigma^2 (Q^T Q)^{-1})^T$  is the same as  $\sigma^2 (Q^T Q)^{-1}$ . The inverse of the matrix  $Q^T Q$  exists, because the problem is well posed (Fabian & De Groot, 2019). The squared standard deviations of the assigned magnetizations are now found on the main diagonal of the  $\sigma^2 (Q^T Q)^{-1}$  matrix. The root of the main diagonal therefore gives the standard deviations of the assigned magnetizations, per  $x$ ,  $y$ ,  $z$ -component.

### 2.3 Coordinate transformations

To simplify the description of the 95% confidence interval, that is constructed by twice the standard deviation as obtained above, we change the coordinate system from Cartesian to spherical. Therefore, we converted the magnetization vector from the Cartesian frame to the spherical frame, where

1. the norm,  $|\mathbf{m}|$ , is given by  $\sqrt{m_x^2 + m_y^2 + m_z^2}$ ,
2. the angle with respect to the  $x$ -axis in the  $xy$ -plane,  $\phi$ , is given by  $\tan^{-1}(m_y/m_x)$ ,
3. and the angle with respect to the  $z$ -axis,  $\theta$ , is given by  $\cos^{-1}(m_z/\sqrt{m_x^2 + m_y^2})$ .

It is complicated to transform the standard deviation describing a Gaussian distribution on the three axes of the Cartesian coordinate frame to a corresponding distribution in spherical coordinates in an analytical way. However, this difficulty can be circumvented numerically by bootstrapping the magnetization vector (Fig. 2). The mean magnetization vector is bootstrapped 10,000 times by drawing samples from a multivariate normal distribution based on both the mean magnetization vector and the complete

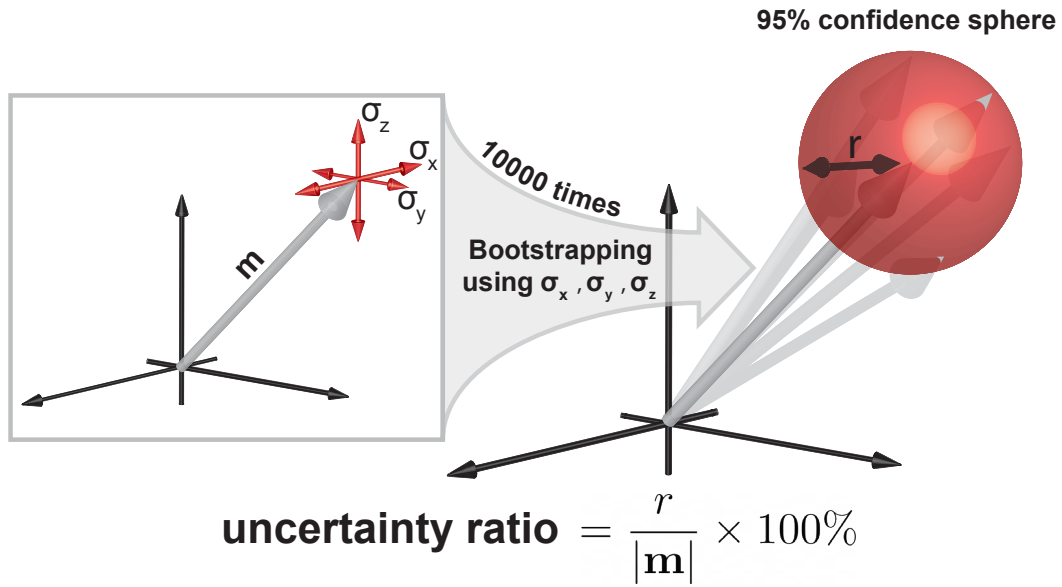


**Figure 2.** The construction of the uncertainty ratio. The standard deviations in the  $x$ ,  $y$ , and  $z$ -directions ( $\sigma_x$ ,  $\sigma_y$ , and  $\sigma_z$ , respectively) are bootstrapped to generate a set of 10,000 possible magnetization vectors around mean magnetization vector  $\mathbf{m}$ . The radius of a sphere containing 9,500 of the end-points of these vectors is defined as the 95% confidence sphere with radius  $r$ . The length of the magnetization vector  $|\mathbf{m}|$  and  $r$  are then used to define the uncertainty ratio of a solution.

covariance matrix. These samples are used to construct difference vectors, which represent the difference between the bootstrapped vectors and the mean magnetization vector in the Cartesian frame. The norms of these vectors are sorted in ascending order and the 9,500th norm value is used as radius,  $r$ , for a 95% confidence sphere. Note that we have implicitly assumed that the bootstrapped magnetization vectors are Fisherian distributed, which means that the deviation from the mean is the same in every direction (Fisher, 1953). However, this is not necessarily true, because the standard deviation in the Cartesian coordinate frame is not equal in the  $x$ ,  $y$ , and  $z$  direction. The real distribution is therefore probably more similar to an elliptic Kent distribution (Kent, 1982). On the other hand, the downside of parametrizing the Kent distribution is that it is necessary to use three parameters to describe an ellipsoid. Nevertheless, the dimension ( $|\mathbf{m}|$ ,  $\theta$ , or  $\phi$ ) in which the uncertainty is mainly concentrated is not important, because if the uncertainty in one dimension turns out to be too large, then the magnetization of the grain cannot be used even if the other two dimensions have small uncertainties. For that reason we assume a Fisherian distribution, which can be visually represented by a 95% confidence sphere around the mean magnetization vector.

The radius of the confidence sphere is an absolute measure. This makes it difficult to compare the magnetization uncertainties of grains with different mean magnetizations. We therefore define the uncertainty ratio as the radius of the 95% confidence sphere,  $r$ , as fraction of the mean magnetization vector  $|\mathbf{m}|$  (Fig. 2):

$$\text{uncertainty ratio} = \frac{r}{|\mathbf{m}|} \times 100\%. \quad (10)$$

## 2.4 Signal strength ratio

The performance of the MMT technique depends on how well the magnetic moment of an individual grain is expressed in the magnetic flux map on the surface of the grain. To assess the potential maximum contribution to the magnetic flux on the surface of the sample arising from an individual grain Cortés-Ortuño et al. (2021) defined the  $V/R^3$  ratio. This property is dependent on the distance of the grain to the scanning surface,  $R$ , and the volume of the grain,  $V$ , (see Appendix of de Groot et al., 2018). Unfortunately, the  $V/R^3$  ratio does not account for the magnetization of grains as function of their volume. Smaller SD to PSD grains have on average stronger magnetizations than larger MD grains (Dunlop, 1990; de Groot et al., 2018). To improve the  $V/R^3$  ratio we

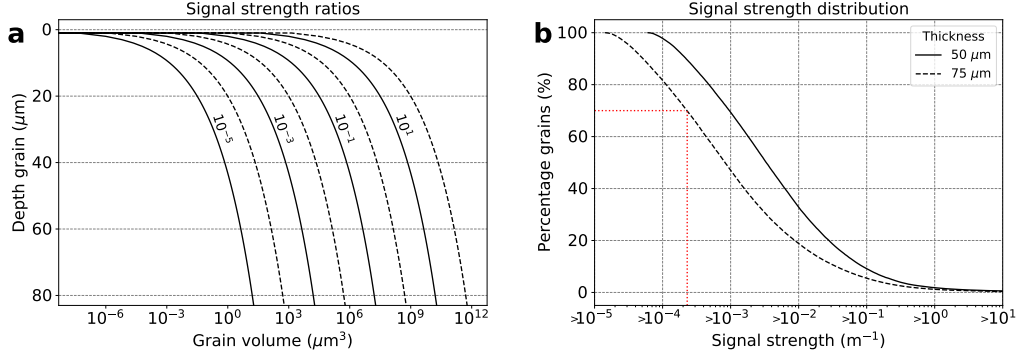


**Figure 3.** a) Relation between grain depth and grain volume as a function of SSR. b) Reversed cumulative SSR distribution for a 50 and 75  $\mu\text{m}$  thick sample based on grains of the volcanic sample of de Groot et al. (2013). This panels shows, for example, that 70% of the grains in a modeled sample with a thickness of 75  $\mu\text{m}$  have a SSR larger than  $2.3 \times 10^{-4}$ , as indicated by the red dotted lines.

used the relation between grain diameter and magnetization as described in equation (1) and defined the signal strength ratio, SSR:

$$\text{SSR} := \frac{V}{R^3 d} = \frac{\pi d^2}{6R^3} = \frac{\sqrt[3]{4\pi V^2}}{2\sqrt[3]{3}R^3}, \quad (11)$$

with  $d$  the diameter of the grain in  $\mu\text{m}$ , assuming that the volume of the grain is shaped like a sphere. de Groot et al. (2021) related the magnetization to the volume of the grains, so the grain's shapes are not taken into account. Fig. 3A shows the effect of the signal strength. It shows that, although smaller grains are now parametrized to produce a stronger signal, larger signal strengths are still linked to predominantly larger grain volumes.

The cumulative distribution of the SSR per model is shown in Fig. 3b. All models use the same randomly selected grains from the volcanic sample, therefore, we only distinguished a SSR distribution for the 50 and 75  $\mu\text{m}$  thick samples, since the thickness of the sample is the only factor influencing the SSR distribution. Because the 75  $\mu\text{m}$  sample contains deeper grains, the minimum SSR for those models is lower than for 50  $\mu\text{m}$  thick models. This trend is also shown by the median SSR, which indicates that approximately 70% of the grains in a 75  $\mu\text{m}$  thick model have a SSR of at least  $2.3 \times 10^{-4}$ . This SSR is obtained, for example, for a grain with a volume of  $10 \mu\text{m}^3$  at a depth of 25  $\mu\text{m}$ . On the other hand, 70% of the grains in a 50  $\mu\text{m}$  thick model have a SSR larger



than  $9.8 \times 10^{-4}$ . A grain with this SSR and a volume of  $10 \mu\text{m}^3$  would be located at a depth of  $16 \mu\text{m}$ .

### 3 Results

First, we present the influence from sample surface size, sample thickness, grain density, noise level, and sampling interval on the uncertainty ratio of the obtained magnetizations. Thereafter we will focus on individual magnetization solution, where we inspect the minimally needed SSR to produce magnetization results with an acceptable uncertainty ratio.

#### 3.1 Uncertainty ratio

##### 3.1.1 Grain density

After running and combining results of all fifteen iterations per model, the sizes of all uncertainty ratios are sorted per noise level and summarized in Fig. 4 for the  $200 \times 200$  and  $500 \times 500 \mu\text{m}^2$  sample surface sizes. We indicate an uncertainty ratio of 10% as a reference size in the panels of this figure, because it is the largest uncertainty value still considered low (*e.g.*, Berndt et al., 2016). A 10% uncertainty ratio means that 9,500 of the 10,000 bootstrapped vectors are located within a sphere which has a radius of 10% of the norm of the mean magnetization vector.

For the samples with a surface size of  $500 \times 500 \mu\text{m}$  and a thickness of  $50 \mu\text{m}$  we observe an exponential increase in uncertainty ratio (Fig. 4e-f). Grain densities smaller than or equal to  $10^4$  grains per  $\text{mm}^3$  are frequently associated with small uncertainty ratios ( $<10\%$ ), which means that most grains in these distributions are relatively well solved. For grain density levels larger than  $25 \times 10^3$  grains per  $\text{mm}^3$ , uncertainty ratios of some grains exceed 100%. Note that these large uncertainties are already retrieved for a scan surface resolution of  $1 \mu\text{m}$ . These large uncertainties potentially mean that some grains in volcanic samples, which have similar grain densities, cannot be resolved well. Fig. 4e shows, however, that the large uncertainty ratios are only obtained for a quarter of the grains with these high grain densities. More than half of the grains still have uncertainty ratios smaller than 1% for the best-case scenario (*i.e.* instrumental noise of 5 nT, sampling interval of  $1 \mu\text{m}$ ). Therefore, most grains can be well solved with a sufficiently small uncertainty.

### 3.1.2 Noise level

Increasing the noise level from 5 to 100 nT results in an overall increase of all uncertainty ratios between one and two orders magnitude (Fig. 4e). These larger uncertainties are expected, because a larger noise level directly increases the standard deviation of the solution through the covariance matrix (see equation 9). The median confidence interval for the highest grain density increases from 0.5% to 10% for a noise level of respectively 5 and 100 nT and the smallest sampling interval, but the median uncertainty ratio for the lowest grain density increases only from 0.01% to about 1%. This shows that the noise level has more influence on the total validity of a high grain density solution than on a low grain density solution, although this trend is partly obscured by the log scale in the figures.

### 3.1.3 Sampling interval

The sampling interval has an exponential effect on the uncertainty ratio, which looks in similar to an intensification of the noise level (Fig. 4e-f). Nevertheless, the increase becomes stagnant between a sampling interval of 4 and 5  $\mu\text{m}$ , but is amplified between a sampling interval of 1 and 2  $\mu\text{m}$  or 2 and 4  $\mu\text{m}$  (Fig. S1a-d in Supplementary Information). This property can be attributed to the relatively smaller decrease in the number of surface magnetic scan points because the amount of points lowers by only 36% when reducing the sampling rate from 4 to 5  $\mu\text{m}$ , yet the amount of points lowers by 75% when reducing the sampling interval from 1 to 2, or from 2 to 4  $\mu\text{m}$ .

The effect of a decreasing sampling rate on the solution uncertainty shows that the increase in uncertainty ratio becomes progressively larger for increasing grain density. Additionally, the combination of elevated noise levels and coarser sampling rates results in median uncertainty ratios over 10% for the largest grain density (Figure 4f). This makes a majority of the grains in such samples difficult to use in subsequent interpretation stages, as the uncertainty increases substantially.

### 3.1.4 Sample thickness

Sample thickness is a major factor that influences the uncertainty ratio. A comparison of panels e against g, and f against h of Fig. 4 shows that for every noise level and sampling interval scenario, the median uncertainty ratios of a majority of grains in-

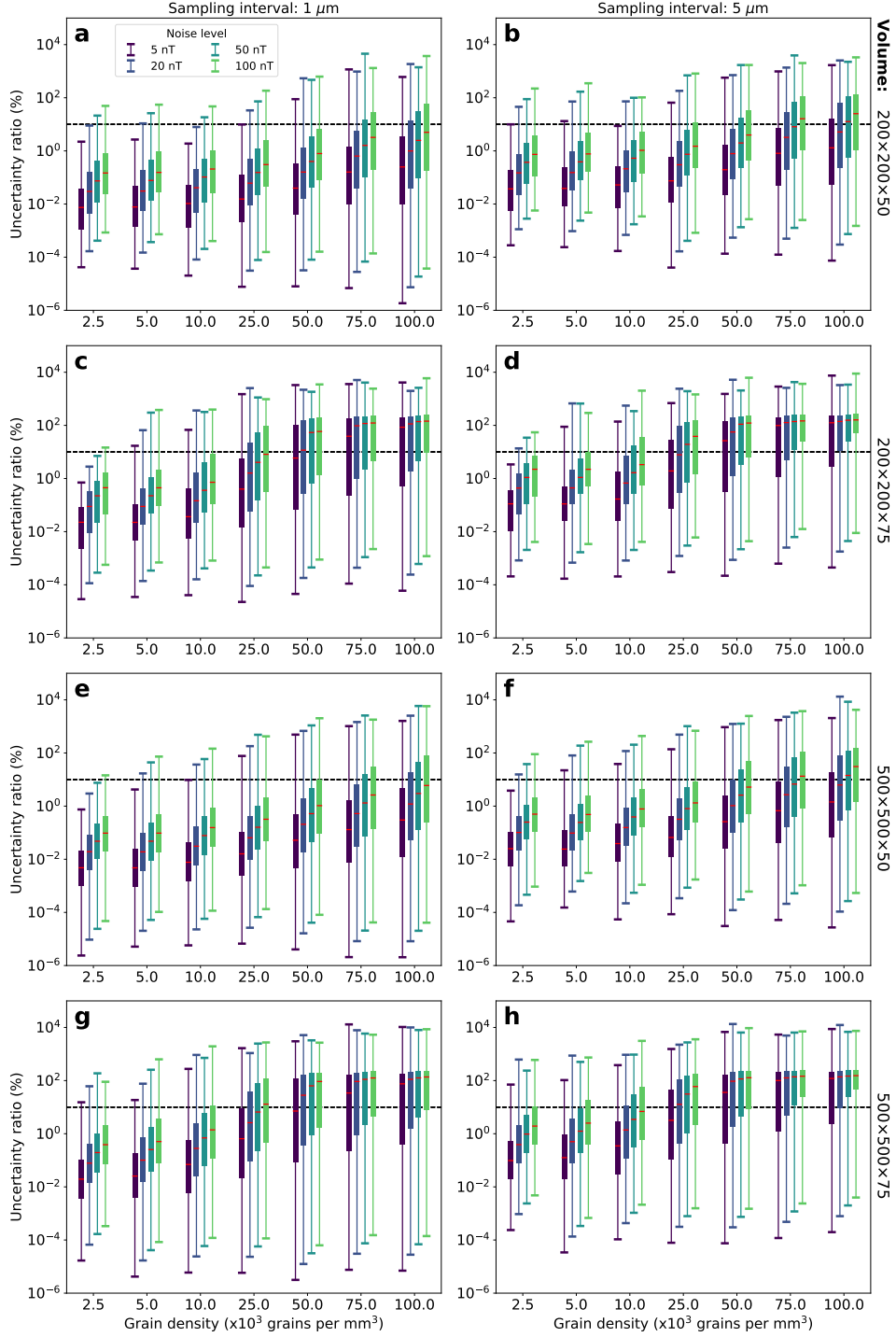


**Figure 4.** Box-plots showing the distribution of the uncertainty ratio as a function of grain density. The set of panels a-d show results for a  $200 \times 200 \mu\text{m}^2$  sample surface and the set of panels e-h show results for a  $500 \times 500 \mu\text{m}^2$  sample surface. Each of the four box-plots per panel per grain density correspond from left to right to one of the four noise levels, respectively 5, 20, 50, and 100 nT. The top panels of each set (a-b and e-f) refer to a  $50 \mu\text{m}$  thick sample. The bottom panels of each set (c-d and g-h) refer to a sample with a thickness of  $75 \mu\text{m}$ . The first column of panels is constructed with a sampling interval of  $1 \mu\text{m}$  and the second column is constructed with a sampling interval of  $5 \mu\text{m}$ .

crease more than one order of magnitude when increasing the sample thickness from 50 to 75  $\mu\text{m}$ . The interquartile range for a grain density of  $25 \times 10^3$  grains per  $\text{mm}^3$  is below 10% for a 50  $\mu\text{m}$  sample, but for a 75  $\mu\text{m}$  sample this range is partly exceeding the 10% already for all sampling intervals. For the high grain density samples ( $> 25 \times 10^3$  grains per  $\text{mm}^3$ ) the effect of a higher sample thickness is more severe, because more than half of their grains have a confidence sphere size of  $\geq 10\%$ . However, low grain density samples ( $< 25 \times 10^3$  grains per  $\text{mm}^3$ ) still have a majority of grains with an uncertainty ratio  $< 10\%$  for every combination of noise level and sampling interval.

The interquartile range in Fig. 4g-h shows an interesting trend when increasing grain density, sampling interval, noise level, and sample thickness. We expect that letting these parameters increase should cause the uncertainty ratio distribution to rise progressively. However, the interquartile range of the confidence interval does not increase, but stagnates when reaching a size of approximately 200%. Fig. 4g-h shows that the maximum uncertainty ratio can become higher than 200%, but the level does not increase anymore when the interquartile range stagnates at 200%. Moreover, after reevaluating the uncertainty ratios for the higher grain densities of the 50  $\mu\text{m}$  sample (Fig. 4e-f), we observe that the maximum confidence interval of the thinner sample stagnates as well when approaching large uncertainties. This might mean that grains do not become progressively worse to solve, but we should not rule out other factors, such as the geometrical consequence of introducing the confidence sphere.

### 3.1.5 Sample surface size

The effect of the sample surface size is small compared to sample thickness. A comparison of the panels a-d and e-h of Fig. 4 indicates that the interquartile range of uncertainty ratios of the 75  $\mu\text{m}$  samples of both domain sizes are very similar. The lowest grain densities of the 75  $\mu\text{m}$  sample show somewhat lower and less scattered uncertainty ratios for the  $200 \times 200 \mu\text{m}^2$  sample surface size than for the same sample in the  $500 \times 500 \mu\text{m}^2$  sample surface. The uncertainty ratio distribution for the larger grain densities of both sample surfaces is on average the same. It is therefore reasonable to assume that the surface area of the sample does not play a major role in determining correct grain magnetizations for most grain densities, but only influences the amount of computational power to solve the inversion, since many more grains and data points in the magnetic surface scan are present.

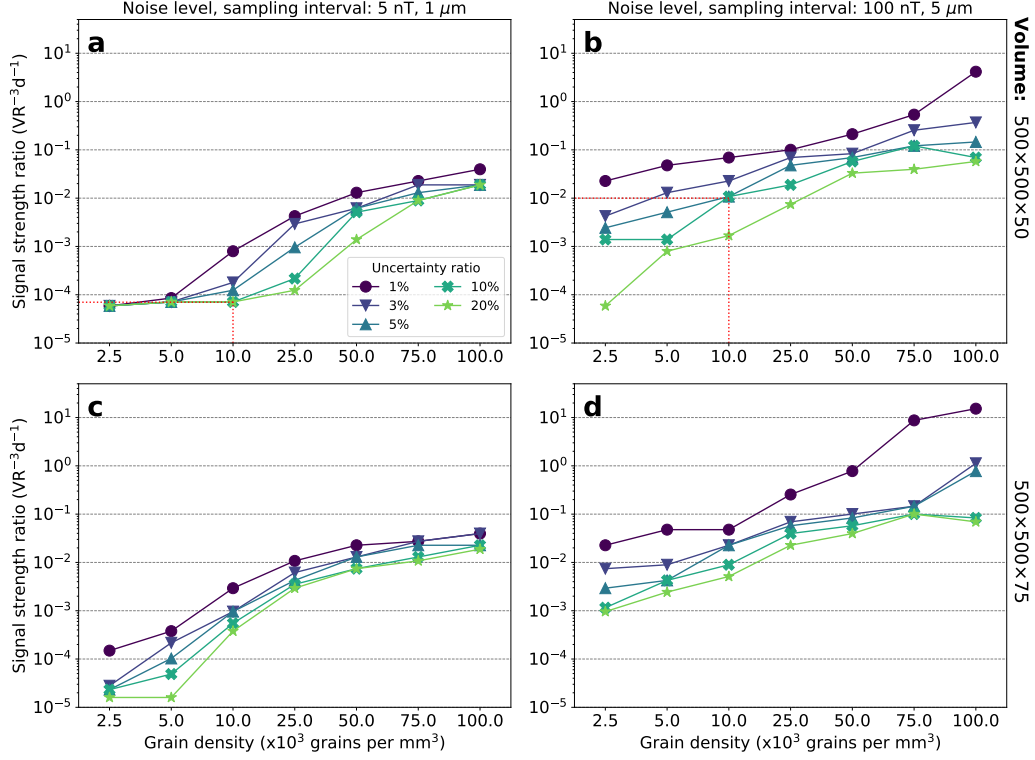


**Figure 5.** Resolved SSR plotted against grain density for different uncertainty ratios for the  $500 \times 500 \mu\text{m}^2$  sample surface. The top row of panels is obtained for a sample thickness of  $50 \mu\text{m}$ . The bottom row of panels is based on a sample thickness of  $75 \mu\text{m}$ . Panels a and c represent results for a noise level of 5 nT and sampling interval of  $1 \mu\text{m}$ . Panels b and d show results for a noise level of 100 nT and sampling interval of  $5 \mu\text{m}$ . Each panel contains five lines corresponding to different uncertainty ratios, namely, 1% (circle), 3% (upper base triangle), 5% (lower base triangle), 10% (cross), and 20% (star). The red dotted lines in panel a and b represent an example described in section 3.2, which shows that the SSR increases from  $7 \times 10^{-5}$  to  $10^{-2}$  when experimental conditions deteriorate for a sample with a grain density of  $10^4$  grains per  $\text{mm}^3$  and 10% uncertainty ratio. These signal strengths corresponds to, *e.g.*, solving a  $10 \mu\text{m}^3$  grains at a depth of 38 and  $7 \mu\text{m}$ , respectively.

### 3.2 Signal strength ratio

Up to this point the distribution of the uncertainty ratios for combinations of different grain densities, noise levels, sampling intervals, sample thicknesses, and sample surface sizes have been assessed. From the results we observe that for samples with high uncertainty (*e.g.* 75  $\mu\text{m}$  thickness and high grain density) it is possible to find small groups of grains with very low uncertainty ratios ( $< 10\%$ ). To determine which grains in a certain model produce acceptable uncertainties, we assess the SSRs as function of the uncertainty ratios of the magnetizations. In Fig. 5 the minimally needed SSR to solve the magnetization of a grain with a certain uncertainty ratio is plotted as function of grain density in the models with a sample surface size of  $500 \times 500 \mu\text{m}^2$ . Each panel in the figure contains five uncertainty ratios, namely, 1%, 3%, 5%, 10%, and 20%.

The panels a-b of Fig. 5 show that up to a grain density of  $10^4$  grains per  $\text{mm}^3$  in a sample with a thickness of 50  $\mu\text{m}$ , SSRs of  $7 \times 10^{-5}$  can be solved within uncertainty ratios as small as 10% for a low noise level and a high sampling resolution. This means, for example, that grains with a volume of  $10 \mu\text{m}^3$  can be solved with an uncertainty ratio of at least 10% at a maximum depth of 38  $\mu\text{m}$ . However, for the worst possible conditions, *i.e.* a noise level of 100 nT and a sampling rate of 5  $\mu\text{m}$ , only grains with a SSR of  $10^{-2}$  can be solved at 10% uncertainty ratio, which corresponds to solving a  $10 \mu\text{m}^3$  volume grain at 7  $\mu\text{m}$  depth. According to Fig. 3b, about 35% of the grains have a SSR equal to or larger than  $10^{-2}$ .

The minimal SSR that can be resolved is rising quickly for grain densities higher than  $10^4$  grains per  $\text{mm}^3$ . For the largest grain density and best-case scenario, *i.e.* a noise level of 5 nT and a sampling rate of 1  $\mu\text{m}$ , SSRs larger than  $2 \times 10^{-2}$  can be solved within an uncertainty ratio of 10%. This SSR corresponds to solving about 25% of total amount of grains in such sample. For example, a grain with a volume of  $10 \mu\text{m}^3$  can only be solved at a depth of 5.7  $\mu\text{m}$  or less. In a worst-case scenario grains with a SSR larger than  $7 \times 10^0$  can be solved for the same grain density and uncertainty ratio. For this scenario, only grains at the sample surface produce a SSR large enough to be properly solved.

The sample thickness is again a major factor determining the minimally needed SSR to solve grains for a given uncertainty ratio as shown by the panels c-d of Fig. 5. Especially the influence on small grain densities for the lowest noise levels and sampling intervals is large. The smallest grain density of  $2.5 \times 10^3$  grains per  $\text{mm}^3$  can only be com-

pletely solved for an uncertainty ratio of at least 20%. Furthermore, the larger grain densities contain few grains that can be solved for the highest noise level and sampling interval. Nevertheless, comparing panels a-b against c-d in Fig. 5 shows that the minimum SSR for the same noise level and sampling interval scenario does not change significantly. This means that a thicker sample does not increase the minimally needed SSR to solve a grain for a given uncertainty ratio, implying that shallow grains are not solved worse due to distortion of the weak signal of deep grains. The reason for solving less grains in thicker samples is, therefore, that less grains have the minimally needed SSR, caused by a changed SSR distribution due to the deeper grains as shown by Fig. 3b.

Decreasing the sample surface size causes a minor drop in minimal resolved SSR for both sample thicknesses (see Supplementary Figs. S5 and S6). The SSR of smaller grain densities decreased the most. This decrease in SSR makes it more likely for samples with grain densities up to  $10^4$  grains per  $\text{mm}^3$  to obtain confidence sphere sizes lower than 10%, even for high noise levels and coarse sampling rate. Additionally, the effect of a smaller sample surface size for the  $75\ \mu\text{m}$  sample is similar to the  $50\ \mu\text{m}$  sample.

## 4 Discussion

### 4.1 Parameter impact on uncertainty

We set up a range of numerical models to investigate the responses of grain density, sampling interval, noise level, sample surface size, and sample thickness on the uncertainty of magnetization solutions. Additionally, we assess which combinations of depth and grain size provide stable results given the changing initial conditions. The overall results indicate that the quality of the solutions is highly dependent on grain density in the sample. The grain density directly increases the amount of variables in the inversion, which leads to an increase in condition number and, therefore, in uncertainties. The grain density enlarges the uncertainty ratio distribution up to four orders of magnitude from the best to the worst case scenario in our models. The uncertainty ratio raises rapidly for grain densities larger than  $10 \times 10^3$  grains per  $\text{mm}^3$ , but the larger grain densities still contain a many grains for which we can obtain a solution with an uncertainty ratio of just 1%.

The effect of noise level and sampling interval on magnetization uncertainty is similar, because they both affect the uncertainty ratio with an increase of up to two orders

of magnitude. Compared to the influence of grain density, however, we perceive the effect of noise level and sampling rate to be less severe over the magnetization uncertainty. The noise level does not have a significant influence because the surface magnetic field has, on average, a strength in the order of  $10^{-6}$  to  $10^{-3}$  T, which is many times larger than the largest realistic noise level of 100 nT (Glenn et al., 2017). In the case of sampling interval, its limited influence can be attributed to the vastly overdetermined inversion system, considering that the system contains at least twice as many knowns than unknowns. Moreover, these two parameters can be directly controlled during the experimental set-up, hence the noise level and sampling interval can be further minimized when needed.

The sample surface size has the smallest effect on the magnetization uncertainty of all parameters tested here, because it does not change the ratio of known magnetic field data and unknown magnetization variables in the inversion. Nevertheless, results show that the smallest grain densities obtain slightly better solutions in smaller domain areas, which can only be attributed to the presence of less unknown magnetization variables in the corresponding inversion.

Sample thickness has a major influence on magnetization uncertainty; the uncertainty can rise up to two orders of magnitude by increasing the sample thickness from 50 to 75  $\mu\text{m}$ . This rise is partly caused by the SSR that quickly becomes lower for the additional deeper grains in the thicker sample (see Fig. 3b). We suggest, therefore, that in the process of sample preparation care should be taken to make the sample as thin as possible. Additionally, the distance between sample and sensor should be as small as possible to retrieve the strongest possible signals. This combined leads to relatively high SSRs, resulting into signals that are well visible above the noise.

## 4.2 Uncertainties in previous MMT studies

In the study of de Groot et al. (2018) MMT was used for the first time to successfully obtain individual magnetizations while making use of scanning superconducting quantum interference device microscopy. They inverted magnetic signals from three subdomains in a synthetically created sample with low grain density, but without providing confidence limits for the solutions. The accuracy of the obtained magnetization solutions



is hence unknown. With the results obtained here, the uncertainties of these magnetization solutions can finally be estimated.

The study focused on solving the magnetization of grains in three subdomains with an average area of  $300 \times 300 \mu\text{m}^2$ , a thickness of  $50 \mu\text{m}$ , and an average grain density close to 2500 grains per  $\text{mm}^3$ . The sampling interval is  $1 \mu\text{m}$  and the height of the SSM sensor above the samples is  $1\text{--}2 \mu\text{m}$ . The noise level of the magnetic field produced by SSM is estimated to be much lower than 5 nT, although positional noise can further increase the noise level (Weiss et al., 2007; Lee et al., 2004). We combined the provided information with the newly acquired results of section 4.1. Based on the assumption that we approximately have a  $200 \times 200 \mu\text{m}^2$  sample surface with a thickness of  $50 \mu\text{m}$  for compatibility, we conclude that the uncertainty ratios of the grains in the study were much smaller than 1% (see Fig. 4a). In the extreme case that positional noise would increase the noise level to an unrealistically high level of 100 nT, grains with a SSR larger  $3.7 \times 10^{-4}$  could still be solved with uncertainty ratios of 1%, which is about 90% of the total amount of grains (see Supplementary Information Fig. S5d). The effect of the additional distance of  $1\text{--}2 \mu\text{m}$  between sample and scanning sensor is not significant, considering that the comparison of panels a and c of Fig. 5 show almost no difference in the minimally needed signal strength to solve a grain with an uncertainty ratio of 1% for a density of 2500 grains per  $\text{mm}^3$ . In conclusion, the magnetization results in de Groot et al. (2018) were obtained with high precision, although to achieve the best possible results special care should be taken to reduce the distance between sample and sensor as much as possible.

### 4.3 Convergence of model results

Although the models have been iterated fifteen times, variations caused by model specific configurations can still persist in the obtained uncertainty ratios and distribution or SSRs. The uncertainties in the uncertainty ratio distribution (Fig. 4) have been estimated by comparing the change in cumulative uncertainty ratio distribution each time after a model has been run. The change in median declines, on average, from 80% after two iterations to less than 5% after fifteen iterations. Extending the amount of iterations appears to have no effect, as the average deviation remains around 5% and does not show a declining trend. The lowest grain densities show the highest deviations in median uncertainty ratio of up to 15%, probably because the confidence interval is averaged over less grains compared to denser samples.

Dense samples show an uncertainty ratio distribution which plateaus when reaching percentages larger than 200% (*e.g.* for grain densities larger than  $10^4$  grains/mm<sup>3</sup> in Fig. 4g-h). We hypothesize that this stagnant behaviour is caused by the geometry of the confidence sphere itself, because we have confirmed that the uncertainty in the Cartesian frame ( $\sigma_x$ ,  $\sigma_y$ , and  $\sigma_z$ ) does not stagnate. Additionally, we verified that the magnetization vector has been bootstrapped sufficiently to obtain a 95% confidence sphere, because the change in uncertainty ratios between two iterations is about 0.1% after 10,000 iterations. Excluding these two factors, it seems that the formation of the confidence sphere itself is responsible for the plateau in uncertainty ratio. Nevertheless, the stagnation of the uncertainty ratio distribution has no major effects on the results, because it occurs at uncertainty levels over 200%. Evidently, all grains associated with such high levels of uncertainty are not to be used in a next interpretation stage.

The SSR distribution exhibits deviations of a quarter of a log scale after fifteen iterations for most sampling intervals, noise levels, and sample thicknesses. The SSR associated with the lowest grain densities changes up to half an order in magnitude, contrary to denser samples that change on average less than a quarter of an order magnitude. Similarly to the uncertainty ratio distribution, lower grain densities have more difficulty to produce a constant signal strength average over the model iterations, because they have less grains to cover all positions in the model within fifteen iterations. It is possible that increasing the number of iterations of the model can improve the convergence of the SSRs of grains with lower grain densities. On the other hand, low grain densities have on average a lower minimal SSR and initially a higher percentage grains that pass the uncertainty ratio. Therefore, an error of a quarter of magnitude that is introduced here will not increase the uncertainty ratio of the majority of the grains such that they become unusable for further analysis. The estimated errors for the higher grain densities, likewise, have little effect on the percentage of grains that can be solved, because the potential raise in minimally needed SSR will only result in the rejection of a very small percentage of grains (see Fig. 5).

#### 4.4 Setting a SSR threshold

The SSR is a powerful statistic to quickly discriminate between grains that are resolved well by the MMT inversion and grains that are not properly resolved. For each MMT inversion it is important to set a useful threshold for the SSR for the specific pur-

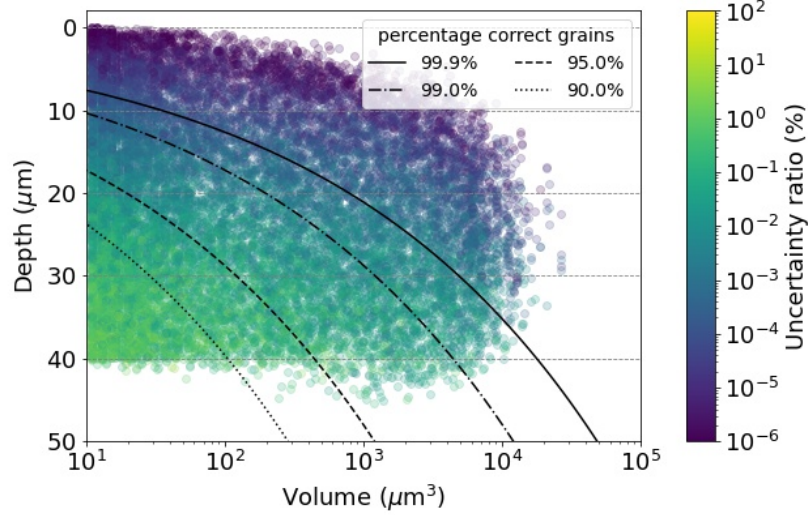


**Figure 6.** Using the SSR to select subsets of grains with accurately resolved magnetizations for our models with a grain density of  $10^5$  grains per  $\text{mm}^3$ , sampling interval of  $1\ \mu\text{m}$ , and noise level of  $5\ \text{nT}$  for a  $500 \times 500 \times 50\ \mu\text{m}$  sample surface. The grains are colored according to their uncertainty ratio. Four different SSRs select 99.9, 99.0, 95.0, and 90.0% of the grains with an uncertainty ratio of maximum 10%.

pose of a study. This threshold depends on the five parameters of the inversions as studied here, and on the required accuracy of the accepted magnetizations. The SSR threshold needs to be balanced between rejecting grains with an accurate solution that do not meet the SSR criterion and including grains that do fulfil the SSR requirements, but are not properly resolved by the inversion. In Fig. 6 we illustrate this based on all grains in the models with dimensions  $500 \times 500 \times 50\ \mu\text{m}$ , a grain density of  $10^5$  grains per  $\text{mm}^3$ , sampling interval in the magnetic scan of  $1\ \mu\text{m}$ , and a magnetic noise level of  $5\ \text{nT}$ . We once again accept a magnetization solution as accurate if the uncertainty ratio is  $<10\%$ . In total there are 18,750 grains in these models, of which 15,301 grains have uncertainty ratios  $<10\%$ ; they would ideally be selected as the accurate subset of grains. We determined SSRs to select sets of grains for which 90.0, 95.0, 99.0, and 99.9% of all accepted grains have an uncertainty ratio  $<10\%$ . When 99.9% of the grains in the subset must fulfill the uncertainty ratio criterion, 6,565 grains are selected using a SSR of  $8.6 \times 10^{-3}$ , i.e. only 42.9% of the desired grains are selected. When 1% of the grains are allowed to violate the uncertainty ratio criterion, the number of grains in the subset increases to

9,342, but 93 of these violate the uncertainty ratio criterion, so 58.0% of the desired grains are recovered by the SSR of  $3.4 \times 10^{-3}$ . For the case where 5% of the grains is allowed to have an uncertainty ratio  $>10\%$ , the SSR of  $7.3 \times 10^{-4}$  accepts 13,863 grains. This implies that although there are 693 grains in this subset that violate the uncertainty ratio criterion, 86.1% of all desired grains are accepted. When 10% badly resolved grains are accepted, 16,289 grains pass the SSR selection of  $2.8 \times 10^{-4}$ , and 95.8% of all properly resolved grains pass, although also 1,629 grains that violate the uncertainty ratio criterion are accepted as well.

The SSR to select a set of accurately resolved grains can be estimated for inversions with different parameters by running computational models with these specific sample dimensions and magnetic scan parameters. Running these additional computational models to determine the best SSR for a specific MMT inversion and purpose of course takes some time, but it is currently the only way to select the most reliable subset of grains after an inversion in a objective way. Moreover, these computational models can also be analyzed before the actual MMT experiments are done based on the parameters that are difficult to control during the experiments (*e.g.* the grain density of the sample). This can help to determine to optimal sample dimensions and boundary conditions for the magnetic surface scans for the MMT experiments.

#### 4.5 Limitations and future research

This modeling study is the first attempt to quantify errors associated with individual magnetization solutions as produced by MMT. We have made, therefore, some simplifying assumptions. First of all, we assumed dipolar magnetization sources for all grains. Most natural grains will not have a dipolar magnetization structure, but a more complex magnetic structure best represented by a multipolar approximation (Butler, 1992; Cortés-Ortuño et al., 2021). The multipolar magnetization of grains could introduce additional uncertainties in the inversion, since the sensitivity to noise of quadrupole, octupole, and higher order magnetization terms is currently unknown. If this sensitivity is negligible, then the results we have derived here would still be valid. However, results from Cortés-Ortuño et al. (2021) show that this assumption is probably not valid, since they showed that the solved magnetization changes when multipole terms are added to the calculation. Also the amount of variables to solve per grain increases when solving for multipole terms, while the amount of data points in the magnetic surface scan does

not increase. Therefore, it would be worthwhile to investigate the sensitivity of these higher order multipole terms to noise, and to study the effect of adding these higher order terms on the uncertainty of the total solution. Fortunately, the magnetic response of multi-domain grains quickly declines with increasing depth, hence we would solely need to model multi-domain grains until a depth of 10 to 20  $\mu\text{m}$  (Cortés-Ortuño et al., 2021).

Furthermore, we assumed that the noise in the magnetic field scan is Gaussian distributed. This assumption is incorrect for natural samples for a couple of reasons. First of all, most grains have a complex multi-domain magnetization structure, but they are solved as if they were in a dipolar state. This means that residuals caused by unsolved higher order magnetic moments will introduce correlated noise to the magnetic surface field. Another source of correlated noise is caused by missing grains or missing parts of grains in the microCT analysis, because the magnetization of these non-inverted parts still has an expression in the surface magnetic field. The influence of the magnetic field expression of non-identified grains on the magnetization solution of other scanned grains is still under research. There is a possibility that the solutions of other grains change if we miss grains that were originally responsible for large signals at the magnetic surface scan.

A third problem that persists within MMT is the limited amount of grains we can invert for at once. Computationally, we can now run an MMT inversion for a sample of  $500 \times 500 \times 75 \mu\text{m}$  and a grain density of  $10^5$  grains per  $\text{mm}^3$ . This requires a computational system with 52 cores and 192 GB of RAM, which enables us to invert for almost 2000 grains at once. Currently, the main limitation for the inversion of larger samples is the RAM capacity of the machine. The RAM requirements can be lowered in the future with further optimizations to the numerical code. Alternatively, it is also possible to reduce the resolution of the scanning grid or reduce the amount of variables by grouping grains when solutions, according to the covariance matrix, are strongly correlated and consequently have a high individual uncertainty ratio. Although this does not decrease the number of data points at the surface, the magnetization uncertainty of the grouped grains is improved and the amount of variables is reduced. Another option is to invert smaller subdomain regions that can be handled by the computational system. Nonetheless, problems will arise in consistency of the magnetization solution of grains near the boundaries of the subdomains, because the subdomains are likely magnetically joint, thereby violating the assumption of magnetic independent regions (Fabian & De Groot,

2019). Nevertheless, the inner grains of the subdomains might still have reliable solutions as long as sufficient information on their produced magnetic surface field is available in the subdomain. Another option is to use a thicker sample, which will immediately increase the number of grains without changing the amount of data points in the magnetic surface scan. However, we have shown that increasing the sample thickness leads to a significant increase in uncertainty ratio, because the deeper grains have an insufficient signal strength to be noticeable at the surface.

## 5 Conclusions

In this study we have acquired a first order estimation of the uncertainties of individual magnetization solutions using MMT. With the help of numerical models we showed that grain density and sample thickness are the major factors influencing the mathematical uncertainty of the magnetization solutions. It is therefore important to make the sample as thin as possible, since the grain density of a sample is often not controlled. Noise level and sampling interval are of secondary importance, because these parameters are controllable during experiments. Moreover, realistic noise levels are very low, and the least squares inversion is vastly over-determined. The sample surface size minimally influences the magnetization results and should only be decreased when the size of the surface magnetic scan leads to overflowing computer memory. It is therefore still difficult to solve for enough grains to obtain a reliable paleointensity or paleodirection. More grains can be solved for by computationally dividing the sample in subdomains to enable the system to solve larger inversion systems. The effects of this procedure on the solution is a topic of ongoing research.

Using the SSR as defined in this study helps to identify individual grains with an accurate magnetic solution as indicated by a low uncertainty ratio, even when a specific combination of the investigated parameters (grain density, noise level, sampling interval, sample surface size, and sample thickness) pose a challenge to the MMT inversion. The SSR is based on volume and depth of a grain, hence it is not necessary to rerun the magnetization inversion to obtain individual uncertainty levels through the covariance matrix. The thresholds for the SSR obtained in this study can, therefore, be applied to other MMT studies that involve the same inversion procedure. In this way we can extract individual well-resolved grains from overall challenging samples and obtain an accurate magnetization solution from only those grains.

We verified that the results for uncertainty ratio distribution and SSR converge within fifteen model iterations. Nevertheless, the stability of magnetization results could be further influenced by other sources of correlated noise, such as undetected grains in the microCT scan or incorrectly solving shallow multi-domain grains using the dipole assumption. The first two sources of errors are difficult to control and model, but the multi-domain grains could be solved with the multipole method of Cortés-Ortuño et al. (2021). In this context, modelling shallow grains with higher order magnetizations will allow to observe the effect of higher order terms on the uncertainty of the individual magnetization solutions in a future study. In summary, by analyzing the effect of five strongly influencing parameters in MMT experiments we have provided a first framework to quantify the uncertainties of the magnetization solutions of natural magnetic grain samples. Consequently, these results can be applied to further paleomagnetic studies to determine the accuracy of obtained natural remanent magnetizations and to individually select reliable grains from bad samples.

## Acknowledgments

Numerical calculations were executed with support of NumPy (Harris et al., 2020), SciPy (Virtanen et al., 2020), and Matplotlib (Hunter, 2007) Python libraries. This project has received funding from the European Research Council (ERC) under the European Union’s Horizon 2020 research and innovation program (Grant agreement No. 851460 to L.V. de Groot).

## References

- Berndt, T., Muxworthy, A. R., & Fabian, K. (2016, 1). Does size matter? Statistical limits of paleomagnetic field reconstruction from small rock specimens. *Journal of Geophysical Research: Solid Earth*, 121(1), 15–26. Retrieved from <https://onlinelibrary.wiley.com/doi/10.1002/2015JB012441> doi: 10.1002/2015JB012441
- Butler, R. F. (1992). *PALEOMAGNETISM: Magnetic Domains to Geologic Terranes*. Boston: Blackwell Scientific Publications.
- Cortés-Ortuño, D., Fabian, K., & de Groot, L. V. (2021, 4). Single Particle Multipole Expansions From Micromagnetic Tomography. *Geochemistry, Geophysics, Geosystems*, 22(4), 7031. Retrieved from <http://>

- 741 [arxiv.org/abs/2101.07010https://onlinelibrary.wiley.com/doi/](https://onlinelibrary.wiley.com/doi/10.1029/2021GC009663)  
 742 [10.1029/2021GC009663http://dx.doi.org/10.1029/2021GC009663](https://onlinelibrary.wiley.com/doi/10.1029/2021GC009663) doi:  
 743 [10.1029/2021GC009663](https://onlinelibrary.wiley.com/doi/10.1029/2021GC009663)
- 744 de Groot, L. V., Biggin, A. J., Dekkers, M. J., Langereis, C. G., & Herrero-Bervera,  
 745 E. (2013, 12). Rapid regional perturbations to the recent global geomag-  
 746 netic decay revealed by a new Hawaiian record. *Nature Communications*,  
 747 *4*(1), 2727. Retrieved from [www.nature.com/naturecommunications](http://www.nature.com/naturecommunications)[http://](http://www.nature.com/articles/ncomms3727)  
 748 [www.nature.com/articles/ncomms3727](http://www.nature.com/articles/ncomms3727) doi: 10.1038/ncomms3727
- 749 de Groot, L. V., Fabian, K., Béguin, A., Kesters, M., Cortés-Ortuño, D., Fu, R.,  
 750 ... Barnhoorn, A. (2021). Micromagnetic Tomography for Paleomag-  
 751 netism and Rock-Magnetism. *Earth and Space Science Open Archive*,  
 752 *44*. Retrieved from <https://doi.org/10.1002/essoar.10507913.1> doi:  
 753 [10.1002/essoar.10507913.1](https://doi.org/10.1002/essoar.10507913.1)
- 754 de Groot, L. V., Fabian, K., Béguin, A., Reith, P., Barnhoorn, A., & Hilgenkamp, H.  
 755 (2018, 4). Determining Individual Particle Magnetizations in Assemblages of  
 756 Micrograins. *Geophysical Research Letters*, *45*(7), 2995–3000. Retrieved from  
 757 <https://onlinelibrary.wiley.com/doi/abs/10.1002/2017GL076634> doi:  
 758 [10.1002/2017GL076634](https://onlinelibrary.wiley.com/doi/abs/10.1002/2017GL076634)
- 759 Dunlop, D. J. (1990, 6). Developments in rock magnetism. *Reports on Progress in*  
 760 *Physics*, *53*(6), 707–792. Retrieved from [https://www.researchgate.net/](https://www.researchgate.net/publication/231090758https://iopscience.iop.org/article/10.1088/0034-4885/53/6/002)  
 761 [publication/231090758https://iopscience.iop.org/article/10.1088/](https://iopscience.iop.org/article/10.1088/0034-4885/53/6/002)  
 762 [0034-4885/53/6/002](https://iopscience.iop.org/article/10.1088/0034-4885/53/6/002) doi: 10.1088/0034-4885/53/6/002
- 763 Dunlop, D. J., & Özdemir, Ö. (1997). *Rock Magnetism*. Cambridge University Press.  
 764 Retrieved from [https://www.cambridge.org/core/product/identifier/](https://www.cambridge.org/core/product/identifier/9780511612794/type/book)  
 765 [9780511612794/type/book](https://www.cambridge.org/core/product/identifier/9780511612794/type/book) doi: 10.1017/cbo9780511612794
- 766 Egli, R., & Heller, F. (2000). *High-resolution imaging using a high-Tc supercon-*  
 767 *ducting quantum interference device (SQUID) magnetometer* (Vol. 105; Tech.  
 768 Rep.). doi: 10.1029/2000JB900192
- 769 Fabian, K. (2000). Acquisition of thermoremanent magnetization in weak magnetic  
 770 fields. *Geophysical Journal International*, *142*(2), 478–486. doi: 10.1046/j.1365-  
 771 -246x.2000.00167.x
- 772 Fabian, K. (2001). A theoretical treatment of paleointensity determination  
 773 experiments on rocks containing pseudo-single or multi domain magnetic



- 774 particles. *Earth and Planetary Science Letters*, 188(1-2), 45-58. doi:  
 775 10.1016/S0012-821X(01)00313-2
- 776 Fabian, K., & De Groot, L. V. (2019, 2). A uniqueness theorem for tomography-  
 777 assisted potential-field inversion. *Geophysical Journal International*, 216(2),  
 778 760–766. Retrieved from <http://arxiv.org/abs/1712.06136>[https://](https://academic.oup.com/gji/article/216/2/760/5151336)  
 779 [academic.oup.com/gji/article/216/2/760/5151336](https://academic.oup.com/gji/article/216/2/760/5151336) doi: 10.1093/gji/  
 780 ggy455
- 781 Farchi, E., Ebert, Y., Farfurnik, D., Haim, G., Shaar, R., & Bar-Gill, N. (2017,  
 782 9). Quantitative Vectorial Magnetic Imaging of Multi-Domain Rock Forming  
 783 Minerals Using Nitrogen-Vacancy Centers in Diamond. *SPIN*, 7(3). doi:  
 784 10.1142/S201032471740015X
- 785 Fisher, R. (1953, 5). Dispersion on a Sphere. *Proceedings of the Royal Society*  
 786 *A: Mathematical, Physical and Engineering Sciences*, 217(1130), 295–305.  
 787 Retrieved from [https://royalsocietypublishing.org/doi/abs/10.1098/](https://royalsocietypublishing.org/doi/abs/10.1098/rspa.1953.0064)  
 788 [rspa.1953.0064](https://royalsocietypublishing.org/doi/abs/10.1098/rspa.1953.0064) doi: 10.1098/rspa.1953.0064
- 789 Glenn, D. R., Fu, R. R., Kehayias, P., Le Sage, D., Lima, E. A., Weiss, B. P., &  
 790 Walsworth, R. L. (2017, 8). Micrometer-scale magnetic imaging of geological  
 791 samples using a quantum diamond microscope. *Geochemistry, Geophysics,*  
 792 *Geosystems*, 18(8), 3254–3267. Retrieved from [https://onlinelibrary](https://onlinelibrary.wiley.com/doi/abs/10.1002/2017GC006946)  
 793 [.wiley.com/doi/abs/10.1002/2017GC006946](https://onlinelibrary.wiley.com/doi/abs/10.1002/2017GC006946) doi: 10.1002/2017GC006946
- 794 Harris, C. R., Millman, K. J., van der Walt, S. J., Gommers, R., Virtanen, P., Cour-  
 795 napeau, D., ... Oliphant, T. E. (2020, 9). Array programming with NumPy.  
 796 *Nature*, 585(7825), 357–362. Retrieved from [http://www.nature.com/](http://www.nature.com/articles/s41586-020-2649-2)  
 797 [articles/s41586-020-2649-2](http://www.nature.com/articles/s41586-020-2649-2) doi: 10.1038/s41586-020-2649-2
- 798 Hunter, J. D. (2007, 5). Matplotlib: A 2D Graphics Environment. *Com-*  
 799 *puting in Science & Engineering*, 9(3), 90–95. Retrieved from [http://](http://nipy.scipy.org/doc/4160265/)  
 800 [nipy.scipy.org/doc/4160265/](http://nipy.scipy.org/doc/4160265/) doi:  
 801 10.1109/MCSE.2007.55
- 802 Kent, J. T. (1982, 9). The Fisher-Bingham Distribution on the Sphere. *Journal*  
 803 *of the Royal Statistical Society: Series B (Methodological)*, 44(1), 71–80. Re-  
 804 trieved from <http://doi.wiley.com/10.1111/j.2517-6161.1982.tb01189.x>  
 805 doi: 10.1111/j.2517-6161.1982.tb01189.x
- 806 Lee, S.-Y., Matthews, J., & Wellstood, F. C. (2004, 6). Position noise in scanning

- superconducting quantum interference device microscopy. *Applied Physics Letters*, 84(24), 5001–5003. Retrieved from <http://aip.scitation.org/doi/10.1063/1.1763215> doi: 10.1063/1.1763215
- Nagy, L., Williams, W., Muxworthy, A. R., Fabian, K., Almeida, T. P., Conbhui, P. O., & Shcherbakov, V. P. (2017). Stability of equidimensional pseudo-single-domain magnetite over billion-year timescales. *Proceedings of the National Academy of Sciences of the United States of America*, 114(39), 10356–10360. doi: 10.1073/pnas.1708344114
- Néel, L. (1955, 4). Some theoretical aspects of rock-magnetism. *Advances in Physics*, 4(14), 191–243. Retrieved from <https://www.tandfonline.com/doi/abs/10.1080/00018735500101204><http://www.tandfonline.com/doi/abs/10.1080/00018735500101204> doi: 10.1080/00018735500101204
- Panovska, S., Korte, M., & Constable, C. G. (2019). One hundred thousand years of geomagnetic field evolution. *Reviews of Geophysics*, 57(4), 1289–1337. doi: <https://doi.org/10.1029/2019RG000656>
- Pavón-Carrasco, F. J., Campuzano, S. A., Rivero-Montero, M., Molina-Cardín, A., Gómez-Paccard, M., & Osete, M. L. (2021). Scha.dif.4k: 4,000 years of paleomagnetic reconstruction for europe and its application for dating. *Journal of Geophysical Research: Solid Earth*, 126(3), e2020JB021237. doi: <https://doi.org/10.1029/2020JB021237>
- Sim, J., & Reid, N. (1999, 2). Statistical Inference by Confidence Intervals: Issues of Interpretation and Utilization. *Physical Therapy*, 79(2), 186–195. Retrieved from <https://academic.oup.com/ptj/article/79/2/186/2837119> doi: 10.1093/ptj/79.2.186
- Snieder, R., & Trampert, J. (1999). Inverse Problems in Geophysics. In *Signal recovery and synthesis* (pp. 119–190). Washington, D.C.: OSA. Retrieved from <https://www.osapublishing.org/abstract.cfm?URI=SRS-2001-SMA2>[http://link.springer.com/10.1007/978-3-7091-2486-4\\_3](http://link.springer.com/10.1007/978-3-7091-2486-4_3) doi: 10.1007/978-3-7091-2486-4{\\_}3
- Tauxe, L., & Yamazaki, T. (2015). Paleointensities. In *Treatise on geophysics* (pp. 461–509). Elsevier. doi: 10.1016/B978-0-444-53802-4.00107-X
- ter Maat, G. W., Pennock, G. M., & de Groot, L. V. (2018). Data descriptor: A chemical, crystallographic and magnetic characterisation of indi-

840       vidual iron-oxide grains in Hawaiian lavas.       *Scientific Data*, 5, 1–9.       doi:  
841       10.1038/sdata.2018.162

842       Virtanen, P., Gommers, R., Oliphant, T. E., Haberland, M., Reddy, T., Cournapeau,  
843       D., . . . van Mulbregt, P. (2020, 3). SciPy 1.0: fundamental algorithms for sci-  
844       entific computing in Python. *Nature Methods*, 17(3), 261–272. Retrieved from  
845       <https://doi.org/10.1038/s41592-019-0686-2>[http://www.nature.com/](http://www.nature.com/articles/s41592-019-0686-2)  
846       [articles/s41592-019-0686-2](https://doi.org/10.1038/s41592-019-0686-2) doi: 10.1038/s41592-019-0686-2

847       Weiss, B. P., Lima, E. A., Fong, L. E., & Baudenbacher, F. J. (2007, 9).       Pale-  
848       omagnetic analysis using SQUID microscopy.       *Journal of Geophysical Re-*  
849       *search*, 112(B9), B09105.       Retrieved from [http://doi.wiley.com/10.1029/](http://doi.wiley.com/10.1029/2007JB004940)  
850       2007JB004940 doi: 10.1029/2007JB004940